tvst

Article

Development of a Preclinical Laser Speckle Contrast Imaging Instrument for Assessing Systemic and Retinal Vascular Function in Small Rodents

Dwani D. Patel[1,2], Al-Hafeez Dhalla[3], Christian Viehland[3], Thomas B. Connor[2], and Daniel M. Lipinski[1,2,4]

[1] Department of Cell Biology, Neurobiology and Anatomy, Medical College of Wisconsin, Milwaukee, WI, USA
[2] Department of Ophthalmology and Visual Science, Medical College of Wisconsin, Milwaukee, WI, USA
[3] Department of Biomedical Engineering, Duke University, Durham, NC, USA
[4] Nuffield Laboratory of Ophthalmology, University of Oxford, Oxford, UK

Correspondence: Daniel M. Lipinski, Department of Cell Biology, Neurobiology and Anatomy, Medical College of Wisconsin, 8701 Watertown Plank Road, Milwaukee, WI 53226, USA.
e-mail: dlipinski@mcw.edu

Received: March 25, 2021
Accepted: July 16, 2021
Published: August 17, 2021

Keywords: LSCI; hemodynamics; non-invasive; retinal blood flow

Citation: Patel DD, Dhalla AH, Viehland C, Connor TB, Lipinski DM. Development of a preclinical laser speckle contrast imaging instrument for assessing systemic and retinal vascular function in small rodents. Transl Vis Sci Technol. 2021;10(9):19, https://doi.org/10.1167/tvst.10.9.19

Purpose: To develop and test a non-contact, contrast-free, retinal laser speckle contrast imaging (LSCI) instrument for use in small rodents to assess vascular anatomy, quantify hemodynamics, and measure physiological changes in response to retinal vascular dysfunction over a wide field of view (FOV).

Methods: A custom LSCI instrument capable of wide-field and non-contact imaging in small rodents was constructed. The effect of camera gain, laser power, and exposure duration on speckle contrast variance was standardized before the repeatability of LSCI measurements was determined in vivo. Finally, the ability of LSCI to detect alterations in local and systemic vascular function was evaluated using a laser-induced branch retinal vein occlusion and isoflurane anesthesia model, respectively.

Results: The LSCI system generates contrast-free maps of retinal blood flow with a 50° FOV at >376 frames per second (fps) and under a short exposure duration (>50 µs) with high reliability (intraclass correlation $R = 0.946$). LSCI was utilized to characterize retinal vascular anatomy affected by laser injury and longitudinally measure alterations in perfusion and blood flow profile. Under varied doses of isoflurane, LSCI could assess cardiac and systemic vascular function, including heart rate, peripheral resistance, contractility, and pulse propagation.

Conclusions: We present a LSCI system for detecting anatomical and physiological changes in retinal and systemic vascular health and function in small rodents.

Translational Relevance: Detecting and quantifying early anatomical and physiological changes in vascular function in animal models of retinal, systemic, and neurodegenerative diseases could strengthen our understanding of disease progression and enable the identification of new prognostic and diagnostic biomarkers for disease management and for assessing treatment efficacies.

Introduction

The growing worldwide public health burden of sight-threatening retinal disorders such as diabetic retinopathy, age-related macular degeneration, and glaucoma urgently necessitates the development of robust diagnostic strategies that facilitate early intervention.[1–3] Specifically, for diseases of vascular etiology, where the onset of vascular dysfunction precedes the development of vision threatening symptoms, oftentimes by decades, the development of imaging modalities that can measure early, presymptomatic changes in vascular function (e.g., blood flow rate, vessel rigidity, pulsatility) may serve to enhance early detection, guide therapy, and help predict disease outcomes.[4–6]

Retinal imaging techniques such as color fundus photography, scanning laser ophthalmoscopy (SLO), and optical coherence tomography (OCT), combined

with procedures such as fluorescein angiography (FA), have enabled multidimensional en face and cross-sectional imaging to resolve critical structural information about the retinal vasculature.[7–10] However, clinical biomarkers observed via these modalities are largely limited to qualitative assessments of vascular health and fail to adequately quantify retinal hemodynamics.[11] Advanced retinal imaging techniques such as OCT-angiography (OCT-A), adaptive optics-SLO (AO-SLO), and Doppler-OCT have begun to elucidate and quantify the relationships between retinal vascular anatomy and function, but each with its own limitations.[12–21] For example, OCT-A offers high resolution and three-dimensional reconstruction of the retinal microvasculature without the use of exogenous contrast agents, but the limited temporal resolution makes it difficult to evaluate blood flow dynamics in slow flow regions.[22] Doppler-OCT is a technique that enables quantitative velocimetry based on OCT, but this method is highly sensitive to the orientation of vessels with respect to the illumination source, complicating its clinical use.[20,21] Moreover, AO-SLO offers unprecedented lateral resolution and may complement OCT-A for resolving the microvasculature, but velocity measurements with AO-SLO are sensitive to vessel orientation and size and are limited to a relatively small field of view (FOV).[11,17,23] Computational tools have been developed to improve retinal blood flow speed mapping in OCT-A and to automate and hasten velocity determinations with AO-SLO, but limitations in temporal resolution and FOV remain to be addressed.[24,25] Therefore, the development and validation of complementary imaging strategies that can not only detect structural changes to the retina but also quantify physiological variations (i.e., changes in retinal hemodynamics) with high temporal resolution and a wide FOV may critically expand the arsenal of tools for studying and monitoring retinal disease.

In this regard, laser speckle contrast imaging (LSCI) is a promising non-invasive and contactless imaging technique capable of generating wide-field maps of blood flow rate without the use of exogenous contrast.[26] In LSCI, illuminating a rigid surface (e.g., a retinal blood vessel) with a coherent light source results in the generation of a random "speckle pattern" where the intensity of each pixel results from the coherent addition of backscattered light with different optical path lengths.[27] Movement within the FOV (e.g., moving blood cells) results in temporal and spatial fluctuations in the speckle pattern such that the rate at which the intensity of each pixel changes over time is characterized by the decorrelation time of the speckle autocorrelation function.[28] When this dynamic speckle pattern is recorded over a finite integration time set by the exposure duration of the camera, the longer integration time relative to the decorrelation time results in a speckle blurring effect, the extent of which is referred to as speckle contrast (K).[27,29] Speckle contrast can be quantified as the ratio of the standard deviation of time integrated speckle intensities to their mean intensity (Equation 1) within a small spatial window of 5×5 or 7×7 pixels (referred herein as "spatial processing") for high temporal resolution or at the same pixel position across time (referred herein as "temporal processing") for high spatial resolution:[26,30]

$$K = \frac{\sigma}{\langle I \rangle} \tag{1}$$

Although the exact relationship between K and the absolute speed (ν) of the scattering particle is nonlinear, speed may be approximated for simplified LSCI analysis as the inverse square of the speckle contrast (Equation 2):[31–34]

$$\nu \approx \frac{1}{K^2} \tag{2}$$

Under these principles, LSCI has been extensively applied for studying cerebral blood flow and is becoming increasingly relevant in ophthalmology.[32,35,36] For example, the XyCam Retinal Imager (Vasoptic Medical Inc., Baltimore, MD) was recently approved by the Food and Drug Administration and is currently in clinical trials.[37] Another commercially available tool based on laser speckle flowgraphy, the LSFG-NAVI (Softcare Co., Ltd., Fukuoka, Japan), has also been clinically applied to monitor progression of diabetic retinopathy, branch retinal vein occlusion (BRVO), and glaucoma.[38–40] However, the development of a LSCI system capable of accurately quantifying early functional changes in retinal hemodynamics may also benefit preclinical studies that rely on small animal models. Specifically, rodents (e.g., mice, rats) are widely used as models of retinal vascular disease, but they typically fail to develop clinically relevant anatomical complications that are characteristic of end-stage human diseases, such as neovascularization, which severely limits their utility for studying disease progression or determining the efficacy of novel therapies.[41,42] Moreover, dysregulation of retinal structure and hemodynamics often manifest in the early stages of Alzheimer's disease, mild cognitive impairment, hypertension, coronary artery disease, and athero-/arterioscelerosis.[43–46] Hence, the ability to reliably quantify retinal vascular function in small animal models may critically benefit preclinical research beyond ophthalmology.

Herein we describe the design of a custom retinal LSCI system built for applications in small rodent models. We subsequently apply retinal LSCI in vivo to demonstrate its ability to characterize anatomical and physiological dysfunction in the context of laser-induced BRVO, and finally apply LSCI to quantify not only changes in retinal hemodynamics but also cardiovascular function in response to varied doses of volatile isoflurane anesthesia.

Methods

Design

Non-Contact Fundus Imaging and Glare Management

Non-contact fundus imaging was a critical design consideration but is difficult to achieve without introducing glare from reflexes off of the cornea and iris. We overcame this challenge by constructing a custom, non-contact LSCI fundus camera that employs both pupil separation and polarization gating to reject reflexes from the cornea and iris. The optical design includes separate illumination and collection optical pathways, combined via a polarizing beam splitter (PBS).

Polarization gating was achieved through the use of a PBS (along with an additional "booster" polarizer to supplement the low extinction ratio of the PBS), which ensured that only crossed polarized light was detected. As specular reflections maintain polarization, but various birefringent and depolarizing structures in the eye will rotate or scramble the polarization[47] (in particular, the retinal nerve fiber layer and retinal pigment epithelium), detecting only cross-polarized light effectively filters out specular reflections from the cornea (as well as optics internal to our camera).

We also employed Gullstrand's separation of pupil principle,[48] in which reflexes from the cornea and iris are avoided by using separate areas of the pupil for illumination and collection. For our LSCI fundus camera, we implemented this principle using ring illumination and collecting through the center of the ring. At the corneal plane, the ring had an inner diameter (ID) of 0.8 mm and outer diameter (OD) of 1.5 mm. Light was collected through the central 0.7-mm diameter of this ring.

Illumination Design

The ring illumination described above was achieved through the use of a custom fiberoptic bundle (Acrolite, Elbridge, NY). A 1-m-long fiberoptic bundle was constructed with 39-µm/0.33-numerical aperture (NA) borosilicate fibers. The distal end was arranged in a 2× stacked ring with OD of 2.13 mm and ID of 1.34 mm, and the proximal end was arranged in a rectangular shape, 2.0 mm wide by 1.0 mm tall, to match the elliptical shape of the laser output (described below).

In designing the illumination system of LSCI instruments, the coherence of the source is critical to ensure optimal speckle contrast.[49] This was particularly true for our system, as multimode propagation through the fiber bundle can reduce spatial coherence and thus speckle contrast.[50] To ensure that we would have sufficient speckle contrast, even despite the use of the multimode fiber bundle, we selected a wavelength stabilized laser (Ondax SureLock; Coherent Inc., Santa Clara CA) operating at 785 nm with 50-MHz linewidth. This wavelength was chosen as it is within the detection spectrum of silicon sensors and because of the availability of high-powered narrow linewidth lasers. The 50-MHz linewidth of this laser corresponds to a bandwidth of approximately 100 frequency modulation (fm), yielding a coherence length of about 6 meters. This long coherence length easily exceeds the modal dispersion in the fiber bundles,[50] which ensures that the field emanating from the fiber bundle remains spatially coherent to maximize speckle contrast.[49] The laser had a maximum output power of 100 mW (before its integrated isolator) and an elliptical output beam size of 0.9 mm × 1.7 mm.

The design of the illumination optics was laid out and optimized in OpticStudio (Zemax, Kirkland, WA), an optical design software. Light emerging from the distal end of the fiberoptic bundle was relayed via a telescope, through a PBS, and into the back focal plane of a Bioptigen G4 mouse imaging bore (Leica Microsystems, Morrisville, NC). The Bioptigen bore is an arrangement of lenses optimized for imaging mouse retina. It is designed to achieve a 50° FOV with 1.7-µm resolution and is optimized and anti-reflective coated for near-infrared (NIR) wavelengths; thus, it was an ideal choice for this application. Leica Microsystems provided a Zemax blackbox of the bore to facilitate the optical design of our probe. An optical schematic of the illumination and collection design is shown in Figure 1. The illumination system includes the distal end of the fiberoptic bundle (L1) and a relay telescope (L2–L4) such that the combined relay telescope and Bioptigen bore had a demagnification of 1.675. With a 0.33-NA illumination fiber bundle, this resulted in a 50° visual angle (1.6-mm arc length) illuminated FOV on the retina, as modeled in Zemax using a murine eye model.[51]

Collection Design

The collection optics of the probe were also optimized in Zemax. A lens (L5) was placed behind the Bioptigen bore such that the focal plane of the

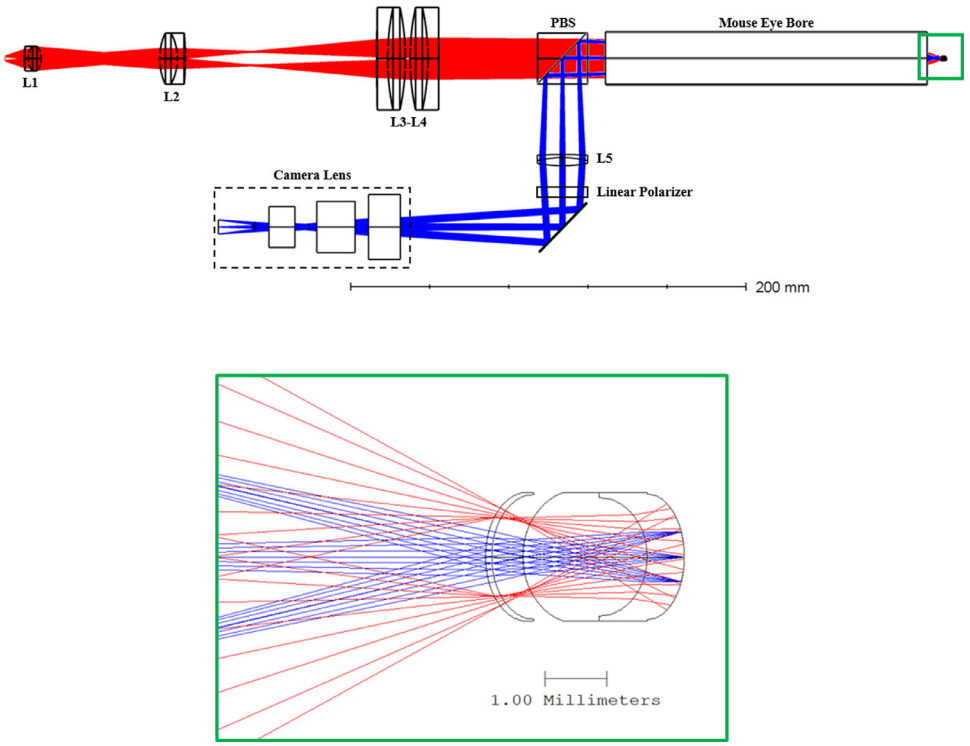

Figure 1. Optical layout of LSCI fundus camera. (*Top*) Optical schematic showing both the illumination (*red*) and collection (*blue*) arms of the LSCI fundus camera. (*Bottom*) Magnified view of illumination (*red*) and collection (*blue*) ray behavior in model mouse eye.

lens was nominally at the back focal plane of the bore. This combination makes the mouse retina appear at infinity, allowing for it to be imaged with a camera lens nominally focused on infinity. A 50-mm *f*/2.0, 6-megapixel (MP), manual focus Navitar camera lens (1-24424; Navitar, Inc., Rochester, NY) was used to focus the image onto an Ace acA2040-180 km NIR camera (2048 × 2048, 180.00 fps; Basler AG, Ahrensburg, Germany). Navitar provided a Zemax blackbox of the camera lens to facilitate the optical design of the probe. To allow for focus adjustment, the position of L5 was then advanced such that the image appeared in the middle of the camera lens focus range (focal distance of 700 mm) instead of on infinity.

Optical Safety Considerations

To ensure that we did not produce any thermal injury to the mouse retina, laser power levels were kept below the Group 1 limits in ANSI z80.36:2016.[52] For our 785-nm light source and a retinal FOV of 50° (1.6-mm arc length on mouse retina, as modeled in Zemax), this limit was computed to be 22.1 mW for exposures up to 2 hours, restricted by the "Retinal infrared radiation thermal hazard" in the standard. Images were nominally acquired with at most 8.35 mW incident on the mouse cornea, as measured with a calibrated power meter (Model 1931-C; Newport Power Meter, Irvine, CA). For all imaging sessions, retinae were exposed for less than 15 seconds.

Animal Purchase and Care

Age-matched male and female C57BL/6J mice (The Jackson Laboratory, Bar Harbor, ME) were housed in the Biomedical Resource Center at the Medical College of Wisconsin under a 12-hour light/dark cycle with food and water ad libitum. All animal protocols were reviewed and approved by the Medical College of Wisconsin Institutional Animal Care and Use Committee and conform with National Institutes of Health and ARVO guidelines for the Care and Use of Laboratory Animals.

In Vivo Mouse Retinal Imaging

In vivo retinal LSCI with our custom system and fundus imaging with the confocal scanning laser ophthalmoscope (cSLO; Heidelberg Engineering, Heidelberg, Germany) were both performed under inhaled anesthesia. Anesthesia was induced using 5% isoflurane in 100% oxygen before being reduced to 2% isoflurane for maintenance. Pupils were dilated using a combination of 2.5% phenylephrine (Paragon BioTeck, Portland, OR) and 1% tropicamide (Akorn,

Lake Forest, IL). Moisture of the eye was maintained during imaging with the use of Systane Ultra lubricant eye drops (Alcon Inc., Fort Worth, TX). Mice were stabilized on an imaging stage with the capability for 2°s of rotation and 3° of translation.

FA was performed 30 seconds following subcutaneous administration of 0.5 mg fluorescein (10% AK-Fluor; Akron Pharmaceuticals, Lake Forest, IL).

Gain, frame rate, frame size, and exposure time for LSCI were controlled through the image acquisition software (XCAP V3.8; Epix Inc., Buffalo Grove, IL). Frame capture rate could be increased from the native 180.00 fps at 2048 × 2048 pixels by subsampling. LSCI at 376.20 fps was achieved by reducing the frame size to 800 × 800 pixels.

Image Processing

Image processing following LSCI was performed as previously described by Patel and Lipinski[26] on MATLAB (MathWorks, Natick, MA) using a custom script to read raw speckle images and generate speckle contrast maps via either temporal processing (for high spatial/low temporal resolution contrast maps) or spatial processing (for high temporal/low spatial resolution contrast maps).[26] Using methods described by Postnov et al.,[35] a custom MATLAB script was also written to perform Fourier analysis in order to segment retinal arteries from veins and to map time delay in pulse wave propagation.

Branch Retinal Vein Occlusion

BRVO was performed in age-matched male and female C57BL/6J mice. Briefly, pupils were dilated using a combination of 2.5% phenylephrine (Paragon BioTeck) and 1% tropicamide (Akorn), mice were sedated following intraperitoneal administration of injectable anesthetic (10 mg/kg xylazine and 60 mg/kg ketamine solution), and moisture of the eyes was maintained using Systane Ultra lubricant eye drops (Alcon Inc.). Vein occlusion was induced by photocoagulation with a green laser diode. Retinal veins were irradiated with a 532-nm diode laser (Iridex, Mountain View, CA) with the following parameters: 100-µm spot size, 200-mW laser power, 0.4-s exposure duration, and four spots per vein. A 5.4-mm fundus contact lens (Ocular Instruments, Bellevue, WA) was used to focus laser light onto the retinal vessel until a white endpoint with vascular narrowing was achieved. Mice were recovered from anesthesia with 5 mg/kg atipamezole.

Results

Assessing the Effect of Mean Pixel Intensity on Mean Speckle Contrast

During LSCI, experimental noise such as variance in mean pixel intensity of raw speckle images resulting from changing exposure durations, laser power, or digitally amplifying light sensitivity of the charged-coupled device sensor of the camera by adjusting gain may affect speckle contrast measurements. Hence, it is important to understand the effects of exposure time, laser power, and gain on mean pixel intensity of raw speckle images and consequently speckle contrast measurements.

In our custom LSCI system, exposure time and gain were adjusted through the image acquisition software, and laser power output was modulated by varying the drive current applied to the laser diode, where current (mA) and laser power (mW) have a linear relationship (Fig. 2A). To understand the influence of mean pixel intensity of raw speckle images on measured speckle contrast, a rigid surface was positioned orthogonally 2.0 cm from the front optical element of the imaging bore, and LSCI was performed at a 3.00-ms exposure duration while varying drive current (35.0–150.0 mA) and gain (0.27–24.08 dB) (Fig. 2B). LSCI under the various gain and drive current settings was repeated at 1.00-ms and 5.00-ms exposure durations to cover the typical range of exposure times applied in our in vivo imaging experiments. For each of the 390 combinations of imaging parameters evaluated, mean speckle contrast was measured in a contrast map generated by temporal processing across 25 consecutive raw speckle images ($N = 12$ sets) and plotted against the mean pixel intensity (0–255 arbitrary units [AU]) measured in the corresponding raw speckle images (Fig. 2C). The effect of mean pixel intensity of raw speckle images on measured speckle contrast may be best described by a multi-order polynomial function, but piecewise linear regression was performed to approximate the range of mean pixel intensities across which mean contrast measurements appeared to plateau before rapidly decreasing to 0 (Fig. 2C). The rate of change in mean speckle contrast measurements with mean pixel intensities was smallest (slope = –7e-5; 95% confidence interval [CI], –9e-5 to –5e-5; $R^2 = 0.9$) between $X_0 =$ 11AU (95% CI, 10–12) and $X_1 = 137$AU (95% CI, 125–144) (Fig. 2C). Consequently, to ensure reproducibility and minimize the influence of raw speckle intensities on speckle contrast measurements during LSCI, mean pixel intensity of raw speckle images should be maintained relatively constant and within X_0 and X_1.

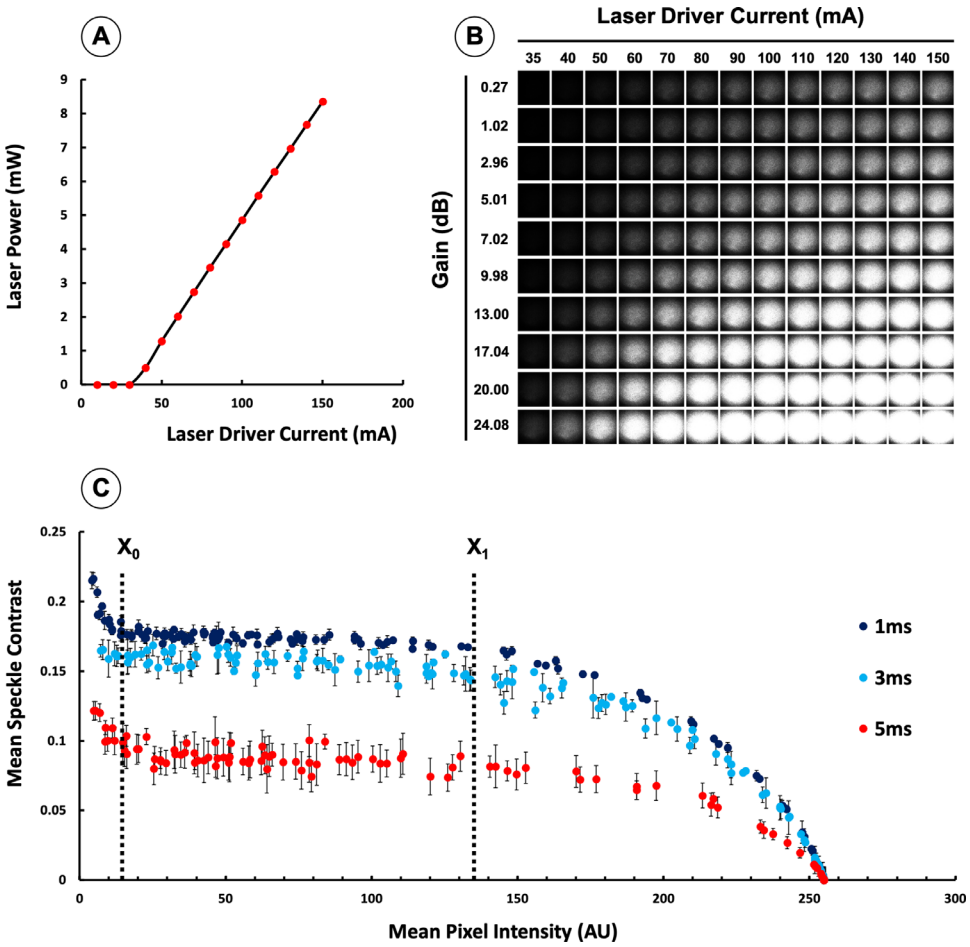

Figure 2. Assessing the effect of mean pixel intensity on mean speckle contrast. (A) Laser power output (mW) can be controlled by adjusting the drive current (mA) applied to the laser diode. (B) A rigid surface was placed 2.0 cm orthogonally from the tip of the imaging bore, and LSCI was performed at 3.00-ms exposure durations at 170.00 fps while varying drive current (35.0–150.0 mA) and gain (0.27–24.08 dB) to alter mean pixel intensity (0–255 AU) of the raw speckle images. LSCI was repeated under 1.00-ms and 5.00-ms exposure durations. (C) For each of the 390 combinations of imaging parameters evaluated, the mean speckle contrast across 25 temporally processed frames ($N = 12$ sets) was plotted against the mean pixel intensity measured across their corresponding raw speckle images. Piecewise linear regression was performed to determine breakpoints in the curve and to identify a range of pixel intensities between $X_0 = 11$ (95% CI, 10–12) and $X_1 = 137$ (95% CI, 125–144) over which change in mean contrast measurements with change in mean pixel intensity of the raw speckle image was smallest (slope, −7e-5; 05% CI, −9e-5 to −5e-5).

Repeatability of Speckle Contrast Measurements In Vivo

Having elucidated the effects of laser power, exposure, and gain on the generation of laser speckle contrast images and having established the ability of our custom system to reproducibly image a static surface under a wide array of conditions, we sought to determine the repeatability of in vivo LSCI measurements in the murine retina. Specifically, as the positioning of experimental animals relative to the LSCI imaging bore—with respect to both distance and angle—is critical to achieving uniform illumination of the retinal surface, we performed a repeatability study wherein raw speckle images ($N = 100$ frames/session) were obtained (170.00 fps, 5.00-ms exposure, and 120.0 mA) over three separate imaging sessions, between each of which positioning of the animal, contact lens (used to prevent corneal desiccation), and x, y, z positions of the imaging stage relative to the bore were reset. Following spatial processing, the average speckle contrast was measured at multiple vessel locations (V1–V5) across the retina for each session (Figs. 3A–3C). Using an intra-rater reliability study, we demonstrated an intraclass correlation coefficient of 0.95 (95% CI, 0.76–0.99) (Fig. 3E), with no statistically significant variance between speckle contrast measurements observed at any vessel location between sessions, indicating a high degree of repeatability.

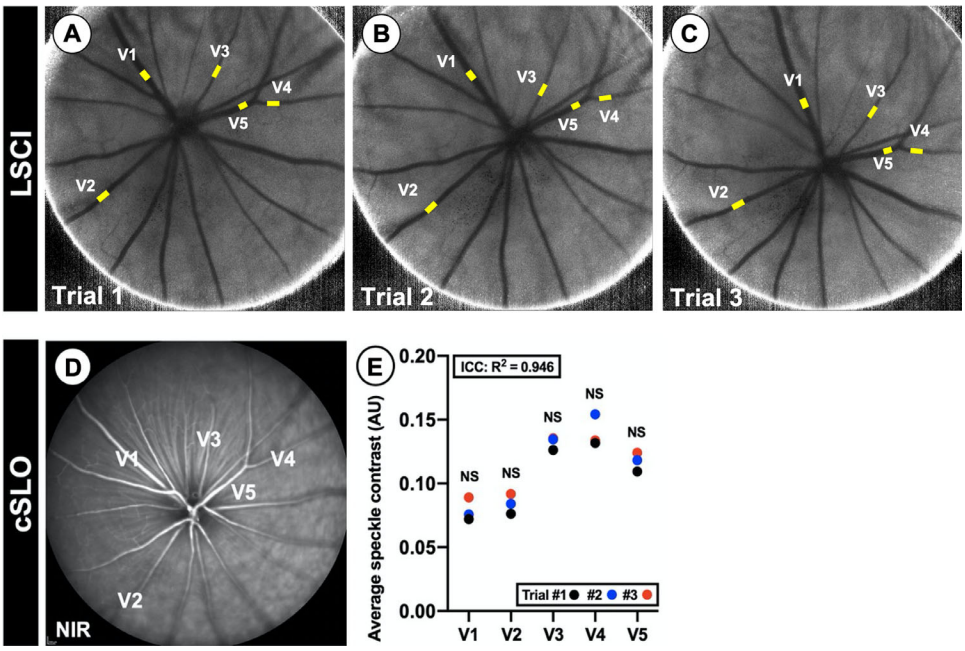

Figure 3. Repeatability of speckle contrast measurements in vivo. (A–C) LSCI was performed at 170.00 fps, 2.50-ms exposure duration, and *f*/16 in a murine eye across three imaging sessions. (D) A representative NIR image of the retina was acquired on a cSLO. Average speckle contrast was measured in each of five vessel regions of interest, and an intra-rater reliability study demonstrated an ICC of 0.946 between speckle contrast measurements within the same retinal vessel ROI across various imaging sessions.

Branch Retinal Vein Occlusion

In order to assess the ability of LSCI to detect pathologic changes in vessel structure and function, we imaged the murine retina ($N = 5$ eyes) with LSCI, FA, and NIR imaging with a cSLO before and then 1, 3, and 14 days after inflicting laser-induced BRVO. Healthy retinae in all eyes were observed to have normal vascular structure before BRVO (Fig. 4A), and arteries and veins could be accurately segmented by Fourier analysis using a technique described in detail by Postnov et al.[35] (Fig. 4B).

NIR imaging 1 day after laser treatment revealed a focal lesion with a hyperreflective center and pale outer ring suggestive of retinal thermal injury (Fig. 4C). FA

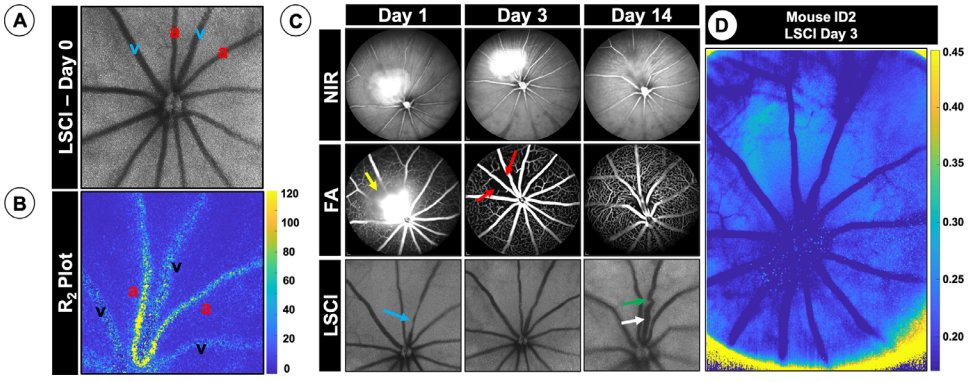

Figure 4. Murine BRVO. BRVO was performed in murine retinae to demonstrate the ability of LSCI to detect pathological alterations in blood flow and retinal vascular anatomy. (A) LSCI was performed 1 day prior to BRVO (170.00 fps, 2.50-ms exposure, and *f*/16). (B) Fourier analysis was applied to segment retinal veins from retinal arteries. (C) The treated mouse was followed for 14 days following BRVO with NIR imaging, FA, and LSCI. Areas of non-perfusion (*yellow arrow*) are seen on FA, and vessel stenosis with distal dilation (*blue arrow*) is evident from LSCI, 1 day after treatment. Likewise, non-perfusion (*red arrows*) is evident via FA on day 3. By day 14, increased tortuosity (*green arrow*) and increased vessel thickness (*white arrow*) are observed upon LSCI. (D) A color map of the speckle contrast image obtained at day 3 reveals increased speckle contrast in areas of the retina which are hypoperfused, correlating with the areas of hypoperfusion observed via FA (C).

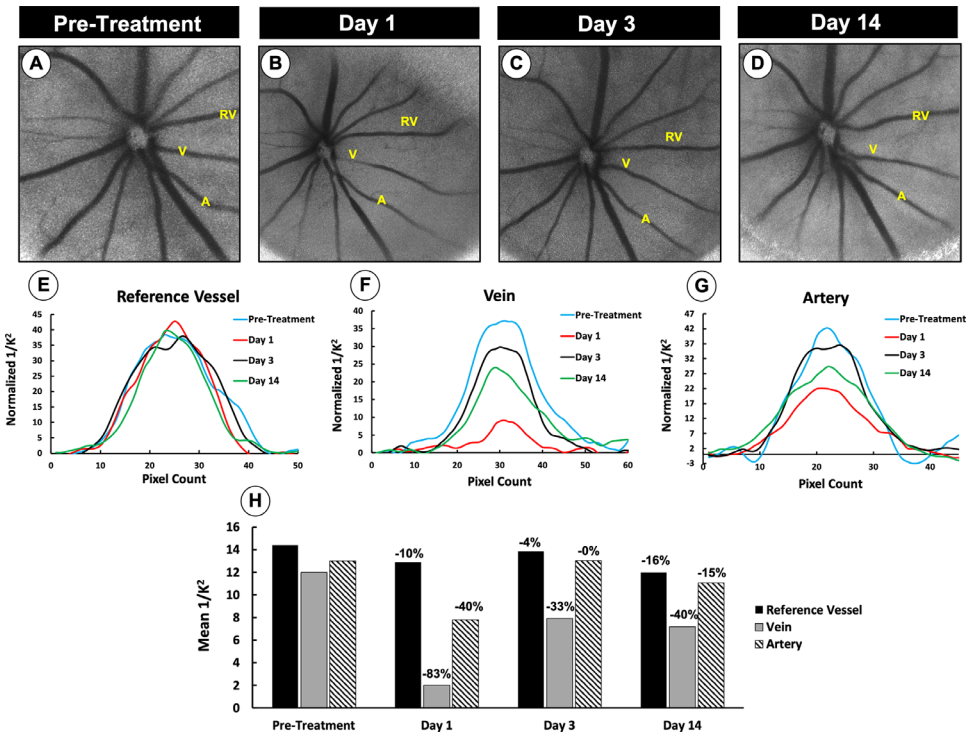

Figure 5. Assessing flow profiles across retinal vessels following BRVO. (A) Fourier analysis was performed in a murine retina to segment retina veins and arteries. (B–E) Speckle contrast–derived flow rates ($1/K^2$) relative to background are assessed across several retinal vessels prior to laser-induced BRVO, and then 1, 3, and 14 days following BRVO. (F–H) Shown are relative flow profiles across a RV, outside of the laser treatment site, as well as a retinal vein and retinal artery within the treatment site. The mean inverse speckle contrast, determined by the mean area under the curve, was measured across RV, V, and A before and then 1, 3, and 14 days after BRVO. (I) Percent change in mean flow rate is shown relative to flow rates measured prior to laser treatment.

revealed hyperfluorescence at the site of laser treatment and in the microenvironment surrounding the affected retinal vessels, indicative of vessel damage. FA also revealed non-perfusion to some arterioles, venules, and capillaries at the site of laser injury (Fig. 4C, yellow arrow). LSCI revealed stenosis (Fig. 4C, blue arrow) on day 1 after laser treatment. On day 3 after laser treatment, NIR imaging showed hyper-reflectivity at the lesion, but notably reduced hyperfluorescence and leakage as confirmed by FA. Although FA and LSCI demonstrated reperfusion and increasing patency of the primary retinal vein at day 3, FA revealed areas of hypoperfusion in smaller retinal vessels of the deeper plexi (Fig. 4C, red arrows). These areas of hypoperfusion could be observed upon LSCI, where areas of increased speckle contrast corresponded to areas with reduced blood flow (Fig. 4D). By day 14, retinal injury and hypopigmentation were evident on NIR imaging; however, blood flow in major retinal arteries and veins appeared unaffected on FA and LSCI. Nevertheless, as highlighted on FA and LSCI, retinal injury, with likely secondary scarring and atrophy, had forced tissue contracture and adduction of retinal vessels towards the affected primary vein (Fig. 4C). Venous dilation (white arrow) and increased tortuosity (green arrow) were also apparent following LSCI.

In order to quantify pathological changes in retinal hemodynamics over the course of disease, speckle contrast derived blood flow rates ($1/K^2$) were assessed across a reference vessel (RV), outside of the laser treatment site, as well as a retinal vein (V) and a retinal artery (A), within the treatment site, prior to laser-induced BRVO and then 1, 3, and 14 days following laser treatment (Figs. 5A–5H). Analysis of mean blood flow rates across these retinal vessels demonstrated that, relative to blood flow rates measured prior to laser-inflicted BRVO, mean flow rate was modestly reduced in RV (−10%) on day 1 after treatment, whereas mean flow rate was more drastically reduced in V (−83%) and A (−40%) (Fig. 5I). Also noticeable on flow profiles was a reduction in the vessel diameter of V on day 1 after treatment (Fig. 5G). Vessel diameters and blood flow rates began to recover across V (−33%) and A (−0%) by day 3; however, by day 14 we observed an overall reduction in blood flow rates across all retinal vessels relative to pre-treatment levels: RV (−16%), V (−40%),

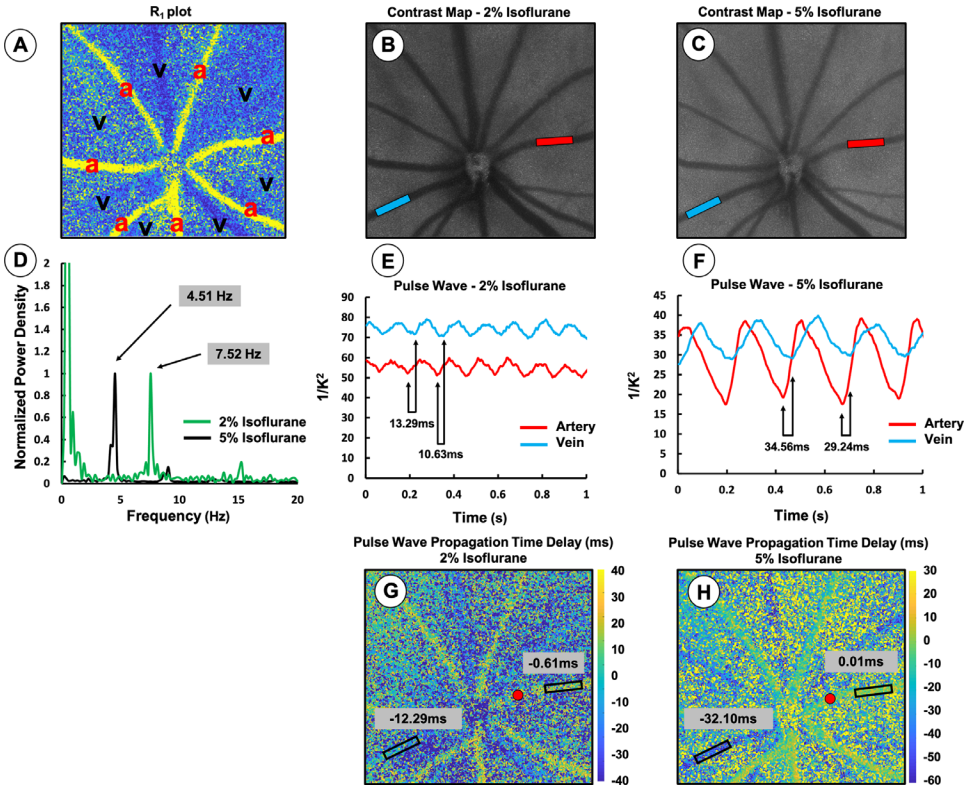

Figure 6. Evaluating cardiac function with LSCI. LSCI was performed in a murine retina at 376.20 fps, 2.50-ms exposure, and *f*/16. (A) Fourier analysis was performed to segment retinal veins from arteries. LSCI was subsequently performed under 2% isoflurane anesthesia (B) and 5% isoflurane anesthesia (C). (D) Fourier analysis was applied to measure change in heart rate under 2% isoflurane (451.20 bpm) and 5% isoflurane (270.60 bpm). Mean speckle contrast was measured in the arterial (*red*) and venous (*blue*) regions of interest drawn in (B) and (C) to plot variation in speckle contrast over time under 2% isoflurane (E) and 5% isoflurane (F). The time delay between pulse wave propagation from retinal artery to retinal vein is highlighted in (E) and (F). Fourier analysis was applied to create a map pulse wave propagation time delay over the entire FOV under 2% isoflurane (G) and 5% isoflurane (H). Time delay measurements in (G) and (H) are relative to time measured in each respective *red* circular region of interest.

and A (−15%) (Figs. 5F–5I). Significant retinal atrophy and tissue contracture on day 14 resulted in compression of retinal vessels. This increase in resistance to flow likely contributed to the overall reduction in mean blood flow rate across all retinal vessels on day 14 (Figs. 5E, 5I). These results showed that the most significant impact of laser treatment for BRVO was on retinal vessels directly within the irradiated area. More specifically, the effect of laser treatment on mean blood flow rate was more prominent on veins than arteries, with the latter demonstrating a quicker recovery over time (Fig. 5I).

Evaluating Murine Cardiac Function with LSCI

A murine retina was imaged at 376.20 fps at 2.50-ms exposure duration, after which Fourier analysis was applied to classify retinal arteries from retinal veins, as described in detail by Postnov et al.[35] (Fig. 6A). The mouse was imaged under 2% isoflurane (Fig. 6B) and 5% isoflurane (Fig. 6C). Fourier analysis on a 2.66-s recording (1000 frames) identified the first harmonic frequency at 4.51 Hz under 5% isoflurane and 7.52 Hz under 2% isoflurane, representing heart rates of 270.60 bpm and 451.20 bpm, respectively (Fig. 6D). Average speckle contrast from an artery and a vein under 2% isoflurane (Fig. 6E) and 5% isoflurane (Fig. 6F) were plotted against time after applying a moving average filter of 15 data points. Fourier analysis revealed an average pulse wave propagation time delay of 11.68 ms under 2% isoflurane (Fig. 6G) and an average pulse wave propagation time delay of 32.11 ms under 5% isoflurane (Fig. 6H), both in agreement with measurements made on respective time-domain, speckle contrast–based pulse wave signals (Figs. 6E, 6F). The temporal variations in the sinusoidal venous flow waveform, upstream of the right atrium, result not only from the forward propagating pulse pressure wave

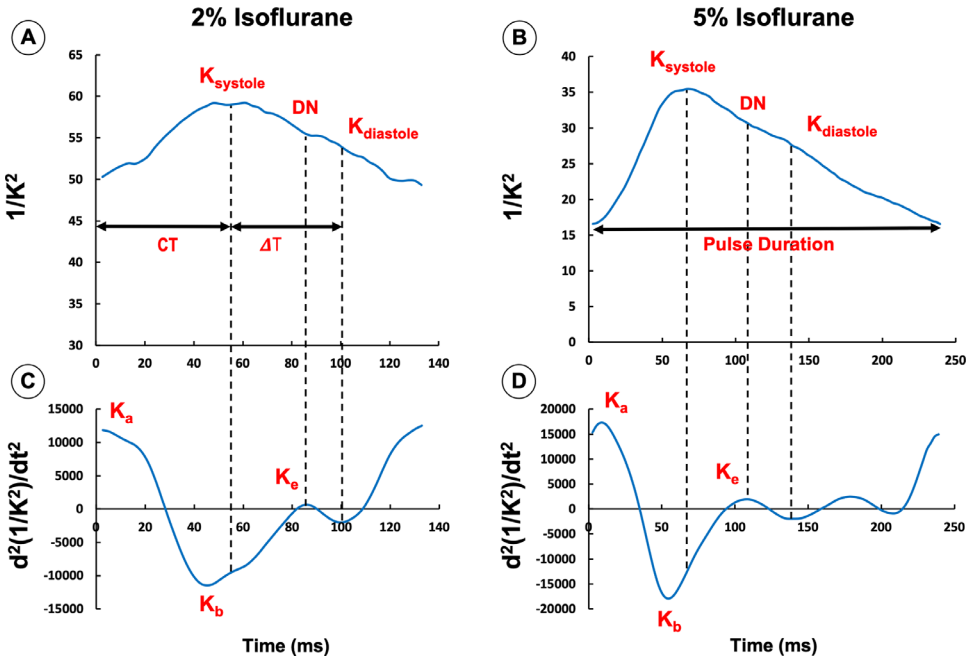

Figure 7. Pulse wave analysis using LSCI. Variation in speckle contrast with cardiac pulsatility results in a waveform that is proportional to pulse waveforms observed on photoplethysmogram. (A, B) The average of five arterial LSCI-based pulse waveforms measured within the same region of interest (see Figs. 6B and 6C) under 2% isoflurane and 5% isoflurane. Here, $K_{systole}$ is the relative speckle contrast–derived flow rate at the peak of systole, $K_{diastole}$ is the relative speckle contrast–derived flow rate at the peak of diastole, DN is the dicrotic notch, ΔT, is the time between $K_{systole}$ and $K_{diastole}$, and CT is the crest time, or the time from the start of the waveform to $K_{systole}$. (C, D) The second derivatives of each averaged waveform. Here, K_a is the early systolic positive wave, K_b is the early systolic negative wave, and K_e is the early diastolic positive wave.

following systole but also from the backward propagating pressure wave from right atrial filling during late diastole.[53] Hence, measuring pulse wave propagation time delays between the arterial and venous circulations may help in evaluating right atrial filling pressures, cardiac contractility, and venous return. Here, the prolonged pulse wave propagation time delay under 5% isoflurane likely reflects the drug-induced delay in ventricular isovolumetric relaxation and left ventricular refilling.[54]

Pulse Wave Analysis Using LSCI

Five arterial blood flow waveforms under 2% isoflurane and five arterial blood flow waveforms under 5% isoflurane were averaged to generate mean speckle contrast–derived blood flow waveforms (Figs. 7A, 7B). The second derivative of each waveform was plotted to identify inflection points in the original waveform, enabling us to easily identify critical parameters that are representative of cardiac function (Figs. 7C, 7D) (Table). By analyzing change in these LSCI-derived parameters between 2% and 5% isoflurane conditions, we were able to characterize the effect of isoflurane anesthesia on murine cardiovascular function. Our evaluation supported previous findings that high-dose isoflurane results in peripheral vasodilation leading to reduced systemic vascular resistance (SVR) and severe hypotension that may be inadequately compensated due to impaired myocardial contractility.[55–57]

First, we found evidence that high-dose isoflurane reduces SVR. The inflection point area (IPA) ratio (A_2/A_1)—where A_1 is the area under the waveform from the start of the pulse wave to the DN and A_2 is the area under the waveform from DN to the end of the pulse wave—is inversely proportional to the SVR.[58,59] A two-tailed Student's *t*-test revealed that the IPA ratio was significantly increased under 5% isoflurane ($P < 0.05$) (Table). Reduced SVR would also slow pulse wave velocities and therefore prolong ΔT, or the time it takes for a pulse pressure wave to travel from the heart to the periphery and back.[58,60] As expected, ΔT was significantly increased under 5% isoflurane ($P < 0.01$) (Table). However, ΔT prolongation may be due to decreased peripheral resistance or increased compliance of large elastic vessels.[58] Herein, we found no significant difference in the parameters associated with large vessel compliance (i.e., CT, early systolic negative wave [K_b]/early systolic positive wave [K_a], and the augmentation index), suggesting that the reduced

Table. Summary of Murine Cardiac Parameters Measured From LSCI-Based Retinal Arterial Pulse Waveforms Under 2% and 5% isoflurane ($N = 5$)

Parameter	Metric	2% Isoflurane	5% Isoflurane	P[a]
IPA ratio (A_2/A_1)	Systemic vascular resistance[58–60]	0.56 ± 0.07	0.93 ± 0.20	<0.05
ΔT, ms	Systemic vascular resistance,[58] large vessel compliance[60]	44.66 ± 8.06	75.49 ± 12.83	<0.01
CT, ms	Large vessel compliance[60,64]	55.29 ± 7.38	66.45 ± 3.26	n.s.
K_b/K_a ratio	Large vessel compliance[60–62]	−1.01 ± 0.09	−1.05 ± 0.11	n.s
Augmentation index, $(K_{systole} - K_{diastole})/K_{systole}$	Large vessel compliance[60,63]	0.55 ± 0.10	0.42 ± 0.10	n.s.
Pulse duration, ms	Duration of cardiac cycle[60]	133.97 ± 1.46	235.51 ± 3.03	<0.0001
Time to DN, ms	Duration of ventricular contraction[60]	85.59 ± 4.76	111.64 ± 12.47	<0.05
Time to diastolic peak, ms	Time to ventricular relaxation[60]	99.95 ± 3.57	141.95 ± 12.69	<0.01
Systolic peak amplitude ($K_{systole}$)	Cardiac output/stroke volume[60]	59.79 ± 1.62	35.57 ± 1.01	<0.0001
Diastolic peak amplitude ($K_{diastole}$)	Cardiac output/venous return[60]	54.29 ± 1.32	27.56 ± 1.99	<0.0001

[a]Significance was determined by two-tailed Student's *t*-test. IPA, inflection point area; CT, crest time; n.s., not significant; DN, dicrotic notch.

SVR was primarily due to peripheral vasodilation and less likely due to changes in large vessel compliance (Table).[60–64]

Furthermore, we observed that cardiac output (CO) was also impaired under high-dose isoflurane. In applying Ohm's law to hemodynamics, we note that blood pressure, which is the driving force for blood flow, is directly proportional to SVR and CO. Hence, to maintain a healthy blood pressure, we expected a reduction in SVR to be compensated by an increase in CO, which is a function of heart rate and stroke volume.[65] However, the reduced heart rate (Fig. 6D) and significantly reduced blood flow rates during peak systole ($K_{systole}$) ($P < 0.0001$) and peak diastole ($K_{diastole}$) ($P < 0.0001$) under 5% isoflurane suggested that high-dose isoflurane led to a reduction in stroke volume, venous return, and an overall reduction in CO.

Finally, high-dose isoflurane may impair myocardial contractility and left ventricular function.[54] Hypotension resulting from the combination of reduced SVR and CO may further compromise coronary autoregulation and consequently impair myocardial contractility.[55] Decreased cardiac contractility was evident through the significantly prolonged pulse duration ($P < 0.0001$) at 5% isoflurane. Meanwhile, a delay in left ventricular isovolumetric relaxation and left ventricular refilling was evident through the significantly prolonged time to DN (closure of the aortic valve; $P < 0.05$) and prolonged time to diastolic peak ($P < 0.01$), respectively (Table).

Discussion

Animal models are widely used to study both ophthalmic and non-ophthalmic diseases with retinal manifestations. As such, the design and optimization of a single, robust retinal LSCI system that can easily be configured for cross-species imaging would be of substantial utility in preclinical research to identify biomarkers of disease progression or measure the efficacy of novel therapies. Herein we detail the optomechanical design of a custom preclinical retinal LSCI instrument capable of producing wide-field fundus images at higher sampling rates (>180 fps with subsampling) and shorter exposure durations (>50 µs) compared with currently available systems, allowing retinal hemodynamics and cardiovascular function to be quantified in small rodents with high spatial and temporal resolution.

Although the principles underlying LSCI have been understood for over four decades and have been applied for in vivo imaging of the retinal vasculature, to date there have been few retinal LSCI systems designed solely for use in small animal models, and those that do exist have design considerations that substantially limit their utility.[66–68] Specifically, previously described systems typically (1) have a rigid optomechanical design (e.g., based on a modified endoscope or fundus camera) that makes configuring the system to accommodate for variations in anatomy, axial length, pupil size, or refractive index across different species challenging or even impossible[69]; (2) are complex to set up or use reproducibly, such as where imaging is dependent upon precise positioning of the animal or illumination fiber in order to generate an image[70]; or (3) are contact instruments involving placement of the front optical element on the corneal surface, which may affect intraocular pressure and therefore blood flow.[26,69,70] In contrast, the instrument described herein is non-contact, largely insensitive to animal positioning relative to the illumination path in order to generate an image of the fundus, and of a flexible optomechanical design that allows the system to be easily modified to account for differences in ocular anatomy, such as axial length or pupil diameter.

Uniquely, by incorporating the imaging bores from the commercially available Bioptigen/Leica OCT system into our design, the instrument could be configured for use in effectively any species simply by exchanging the front optical element for the relevant species-specific bore and making minor adjustments to optics in the illumination arm to ensure light is guided correctly through the pupil without inducing corneal reflections.

Previously we demonstrated that a commercial fundus camera (Phoenix Micron IV) could be converted into a LSCI instrument for use in mice, but we found that there was insufficient laser power to collect short-exposure (<4 ms) images and that the relatively low sampling rate (up to 30 fps) of the native camera severely limited temporal resolution.[26] As this effectively precluded measurement of critical time-varying metrics of retinal and cardiovascular function in the mouse, where heart rates may vary from 500 to 700 bpm in the awake state, a critical consideration in the design of this instrument was the incorporation of a tunable, high-powered (100 mW) volume-holographic-grating–stabilized laser to ensure a high degree of spatial coherence through the ring-fiber bundle and sufficient power at the retinal surface to allow imaging over a wide range of exposures (50 µs–10 s) coupled with a camera capable of capturing high-resolution (2048 × 2048) images at an extremely high frame rate (>180 fps with subsampling).[26,71] The flexibility to independently tune laser power to allow for imaging at varying exposure durations and frame rates is particularly important in the context of works by Chen,[74] who demonstrated that sensitivity to high velocity was best at shorter exposure times and sensitivity to slow flow improved with increasing exposure times. Importantly, the greater temporal resolution of our retinal LSCI system relative to commercially available clinical (<82 fps) and preclinical systems (<30 fps) could be exploited to sample blood flow dynamics over multiple murine cardiac cycles (Figs. 6B–6F).[37,72] Moreover, as pulsatile speckle contrast measurements are well correlated with pulse waveforms detected by photoplethysmography, we were able to extract critical time-varying parameters of systemic vascular and cardiac health (i.e., heart rate, pulse wave propagation time delay, cardiac contractility, vessel stiffness, and peripheral resistance) from the LSCI-derived blood flow waveforms (Table).[73] Although such measurements have recently been derived using LSCI of the retina in human subjects, where the heart rate is substantially slower and so does not require image acquisition at such high frame rates to detect, to the authors' knowledge this represents the first example of these parameters being measured using retinal LSCI in a small animal model.[37]

Although the LSCI instrument described herein represents an advancement over previous systems for preclinical animal use, there remain several critical limitations that must be addressed through improvements in either optomechanical design or image processing. First, using LSCI we can reproducibly measure *relative* changes in bulk flow longitudinally and across multiple vessels simultaneously (Fig. 5), but the inability to obtain *absolute* measurements of particle speed remains a critical limitation, especially if performing repetitive measurements over time to monitor the progression of a disease or response to therapeutic outcome. A partial solution to this deficiency may be to apply a multi-exposure imaging strategy, wherein several series of images are taken at different exposures and the measurements of speckle contrast combined, which was demonstrated by Parthasarathy et al.[32] to significantly improve the linearity between relative changes in speckle contrast-based estimates of flow rate and absolute particle speed when performed across the range of exposures (e.g., 50 µs–80 ms). Whereas this would improve the accuracy of flow rate measurements, it would also necessarily reduce temporal resolution and increase processing burden by requiring the collection of multiple datasets, although this may not be a significant consideration, especially if using LSCI to monitor a chronic disease that progresses over the course of months or years. Another potential strategy to improve the accuracy of LSCI-based flow rate measurements would be to derive a standardized scale of speckle contrast relative to flow velocity by comparing speckle intensity to absolute particle velocity within specific vessels as calculated using other advanced imaging modalities such as AO-SLO, which has demonstrated the ability to quantify single cell velocities across the full range of retinal vessels, from capillaries to primary arteries and veins.[24,75–77] Although automated analysis workflows have simplified the lengthy and laborious process of determining cell velocities with AO-SLO, the limited FOV still requires flow analysis to be performed on a vessel-by-vessel basis.[76] A side-by-side comparison of LSCI and AO-SLO would enable LSCI-based measurements of speckle intensity to be related directly to flow velocity (at least within the individual animal) and would allow quantitative measurements of flow in vessels across the whole retina without montaging.

Although the BRVO model demonstrated that LSCI offers a superior signal-to-noise ratio for visualizing and characterizing vascular structure in the presence of significant hyper-reflectivity and fluorescein leakage, a second obvious limitation of the existing LSCI system relative to other imaging modalities (e.g., FA, OCT-A)

is the inadequate resolution of secondary and tertiary retinal blood vessels, which would be important for assessing areas of hypoperfusion and capillary dropout in models of diseases such as diabetes. One potential way of increasing resolution would be to correct for optical aberrations in the lens and cornea through the incorporation of an adaptive mirror into the collection arm. Although this would be expected to significantly improve resolution of smaller vessels it would add substantial complexity and cost to the existing system, especially if requiring the inclusion of a wavefront sensor, and it would likely result in a reduced FOV. An alternative software-based solution would be the introduction of an processing step similar to the variable interscan time analysis algorithm that has been used to enhance the ability of OCT-A to quantify and present relative changes in blood flow speed.[25,78] Specifically, a similar approach could be applied to LSCI by scaling the smallest and largest detectable speckle contrast values to generate a color-coded map of relative blood flow speed, enabling the detection of hypoperfusion that correlates with areas of capillary dropout (demonstrated in Fig. 4D) but without a comparable spatial resolution to OCT-A.

In summary, despite some limitations related to the measurements of absolute flow rate and the resolution of smaller vessels that will require further system optimization, the custom LSCI instrument described herein represents a versatile tool for detecting hemodynamic alterations in both the local and systemic circulation that can be applied to potentially any preclinical animal model.

Acknowledgments

The authors thank Joseph Carroll, PhD, for assistance in the construction of the custom laser speckle contrast imaging device. The authors also thank Bob Hart of Leica Microsystems and Chuck Rafoth of Navitar for providing the Zemax blackboxes required to facilitate optical design of our probe.

Supported in part by the National Eye Institute under award numbers R01EY027767 and T32EY014537 and by the National Institute of General Medical Sciences under award number T32GM080202. This investigation was conducted in part in a facility constructed with support from a Research Facilities Improvement Program grant (C06RR016511) from the National Center for Research Resources of the National Institutes of Health. The content is solely the responsibility of the authors and does not necessarily represent the official views of the National Institutes of Health. Additional support was provided by a McPherson Eye Research Institute Vision Research Trainee Grant (D.D.P.).

Disclosure: **D.D. Patel**, (P); **A.-H. Dhalla**, (P); **C. Viehland**, (P); **T.B. Connor**, None; **D.M. Lipinski**, (P)

References

1. Brand CS. Management of retinal vascular diseases: a patient-centric approach. *Eye (Lond).* 2012;26(suppl 2):S1–S16.
2. Centers for Disease Control and Prevention. Vision Health Initiative (VHI): common eye disorders and diseases. Available at: https://www.cdc.gov/visionhealth/basics/ced/index.html. Accessed July 30, 2021.
3. Yau JWY, Rogers SL, Kawasaki R, et al. Global prevalence and major risk factors of diabetic retinopathy. *Diabetes Care.* 2012;35(3):556–564.
4. Tayyari F, Khuu L-A, Flanagan JG, Singer S, Brent MH, Hudson C. Retinal blood flow and retinal blood oxygen saturation in mild to moderate diabetic retinopathy. *Invest Ophthalmol Vis Sci.* 2015;56(11):6796–6800.
5. Trivli A, Koliarakis I, Terzidou C, et al. Normal-tension glaucoma: pathogenesis and genetics (review). *Exp Ther Med.* 2019;17(1):563–574.
6. Shin ES, Sorenson CM, Sheibani N. Diabetes and retinal vascular dysfunction. *J Ophthalmic Vis Res.* 2014;9(3):362–373.
7. Novais EA, Baumal CR, Sarraf D, Freund KB, Duker JS. Multimodal imaging in retinal disease: a consensus definition. *Ophthalmic Surg Lasers Imaging Retina.* 2016;47(3):201–205.
8. Tan CSH, Chew MCY, Lim LWY, Sadda SR. Advances in retinal imaging for diabetic retinopathy and diabetic macular edema. *Indian J Ophthalmol.* 2016;64(1):76–83.
9. Fischer J, Otto T, Delori F, Pace L, Staurenghi G. Scanning laser ophthalmoscopy (SLO). In: Bille JF, ed. *High Resolution Imaging in Microscopy and Ophthalmology*. Basel, Switzerland: Springer International Publishing; 2019;35–57.
10. Leitgeb R, Hitzenberger C, Fercher A. Performance of Fourier domain vs time domain optical coherence tomography. *Opt Express.* 2003;11(3):889–894.
11. Li Y, Xia X, Paulus YM. Advances in retinal optical imaging. *Photonics.* 2018;5(2):9.
12. Gao SS, Jia Y, Zhang M, et al. Optical coherence tomography angiography. *Invest Ophthalmol Vis Sci.* 2016;57(9):OCT27–OCT36.

13. Nagiel A, Sadda SVR, Sarraf D. A promising future for optical coherence tomography angiography. *JAMA Ophthalmol.* 2015;133(6):629–630.
14. Spaide RF, Klancnik JM, Cooney MJ. Retinal vascular layers imaged by fluorescein angiography and optical coherence tomography angiography. *JAMA Ophthalmol.* 2015;133(1):45–50.
15. Chalam KV, Sambhav K. Optical coherence tomography angiography in retinal diseases. *J Ophthalmic Vis Res*. 2016;11(1):84–92.
16. Coscas GJ, Lupidi M, Coscas F, Cagini C, Souied EH. Optical coherence tomography angiography versus traditional multimodal imaging in assessing the activity of exudative age-related macular degeneration: a new diagnostic challenge. *Retina.* 2015;35(11):2219–2228.
17. Kaizu Y, Nakao S, Wada I, et al. Imaging of retinal vascular layers: adaptive optics scanning laser ophthalmoscopy versus optical coherence tomography angiography. *Transl Vis Sci Technol.* 2017;6(5):2.
18. Godara P, Dubis AM, Roorda A, Duncan JL, Carroll J. Adaptive optics retinal imaging: emerging clinical applications. *Optom Vis Sci*. 2010;87(12):930–941.
19. Carroll J, Kay DB, Scoles D, Dubra A, Lombardo M. Adaptive optics retinal imaging-clinical opportunities and challenges. *Curr Eye Res.* 2013;38(7):709–721.
20. Leitgeb RA, Werkmeister RM, Blatter C, Schmetterer L. Doppler optical coherence tomography. *Prog Retin Eye Res.* 2014;41(100):26–43.
21. Hendargo HC, McNabb RP, Dhalla A-H, Shepherd N, Izatt JA. Doppler velocity detection limitations in spectrometer-based versus swept-source optical coherence tomography. *Biomed Opt Express.* 2011;2(8):2175–2188.
22. Sambhav K, Grover S, Chalam KV. The application of optical coherence tomography angiography in retinal diseases. *Surv Ophthalmol.* 2017;62(6):838–866.
23. Zhong Z, Petrig BL, Qi X, Burns SA. In vivo measurement of erythrocyte velocity and retinal blood flow using adaptive optics scanning laser ophthalmoscopy. *Opt Express.* 2008;16(17):12746–12756.
24. Joseph A, Guevara-Torres A, Schallek J. Imaging single-cell blood flow in the smallest to largest vessels in the living retina. *Elife.* 2019;8:e45077.
25. Arya M, Rashad R, Sorour O, Moult EM, Fujimoto JG, Waheed NK. Optical coherence tomography angiography (OCTA) flow speed mapping technology for retinal diseases. *Expert Rev Med Devices.* 2018;15(12):875–882.
26. Patel DD, Lipinski DM. Validating a low-cost laser speckle contrast imaging system as a quantitative tool for assessing retinal vascular function. *Sci Rep.* 2020;10(1):7177.
27. Fercher AF, Briers JD. Flow visualization by means of single-exposure speckle photography. *Opt Commun.* 1981;37(5):326–330.
28. Draijer M, Hondebrink E, van Leeuwen T, Steenbergen W. Review of laser speckle contrast techniques for visualizing tissue perfusion. *Lasers Med Sci.* 2009;24(4):639–651.
29. Tokayer J, Jia Y, Dhalla A-H, Huang D. Blood flow velocity quantification using split-spectrum amplitude-decorrelation angiography with optical coherence tomography. *Biomed Opt Express.* 2013;4(10):1909–1924.
30. Duncan DD, Kirkpatrick SJ, Wang RK. Statistics of local speckle contrast. *J Opt Soc Am A Opt Image Sci Vis.* 2008;25(1):9–15.
31. Cheng H, Duong TQ. Simplified laser-speckle-imaging analysis method and its application to retinal blood flow imaging. *Opt Lett.* 2007;32(15):2188–2190.
32. Parthasarathy AB, Tom WJ, Gopal A, Zhang X, Dunn AK. Robust flow measurement with multi-exposure speckle imaging. *Opt Express.* 2008;16(3):1975–1989.
33. Bonner R, Nossal R. Model for laser Doppler measurements of blood flow in tissue. *Appl Opt.* 1981;20(12):2097–2107.
34. Briers JD. Some applications of holographic interferometry and speckle correlation techniques to the study of plant growth and physiology. London: Imperial College London; 1975. Thesis.
35. Postnov DD, Erdener SE, Kilic K, Boas DA. Cardiac pulsatility mapping and vessel type identification using laser speckle contrast imaging. *Biomed Opt Express.* 2018;9(12):6388–6397.
36. Dunn AK. Laser speckle contrast imaging of cerebral blood flow. *Ann Biomed Eng.* 2012;40(2):367–377.
37. Cho KA, Rege A, Jing Y, et al. Portable, non-invasive video imaging of retinal blood flow dynamics. *Sci Rep.* 2020;10(1):1–11.
38. Nakazawa T, Yokoyama Y, Chiba N, et al. Reproducibility of retinal circulation measurements obtained using laser speckle flowgraphy-NAVI in patients with glaucoma. *Clin Ophthalmol.* 2011;5:1171–1176.
39. Nitta F, Kunikata H, Aizawa N, et al. The effect of intravitreal bevacizumab on ocular blood flow in diabetic retinopathy and branch retinal vein occlusion as measured by laser speckle flowgraphy. *Clin Ophthalmol.* 2014;8:1119–1127.
40. Noma H, Yasuda K, Minezaki T, Watarai S, Shimura M. Changes of retinal flow volume after

intravitreal injection of bevacizumab in branch retinal vein occlusion with macular edema: a case series. *BMC Ophthalmol.* 2016;16:61.
41. Robinson R, Barathi VA, Chaurasia SS, Wong TY, Kern TS. Update on animal models of diabetic retinopathy: from molecular approaches to mice and higher mammals. *Dis Model Mech.* 2012;5(4):444–456.
42. Fletcher EL, Jobling AI, Vessey KA, Luu C, Guymer RH, Baird PN. Animal models of retinal disease. *Prog Mol Biol Transl Sci.* 2011;100:211–286.
43. Flammer J, Konieczka K, Bruno RM, Virdis A, Flammer AJ, Taddei S. The eye and the heart. *Eur Heart J.* 2013;34(17):1270–1278.
44. Berisha F, Feke GT, Trempe CL, McMeel JW, Schepens CL. Retinal abnormalities in early Alzheimer's disease. *Invest Ophthalmol Vis Sci.* 2007;48(5):2285–2289.
45. Feke GT, Hyman BT, Stern RA, Pasquale LR. Retinal blood flow in mild cognitive impairment and Alzheimer's disease. *Alzheimers Dement.* 2015;1(2):144–151.
46. Robinson F, Riva CE, Grunwald JE, Petrig BL, Sinclair SH. Retinal blood flow autoregulation in response to an acute increase in blood pressure. *Invest Ophthalmol Vis Sci.* 1986;27(5):722–726.
47. Pircher M, Hitzenberger CK, Schmidt-Erfurth U. Polarization sensitive optical coherence tomography in the human eye. *Prog Retin Eye Res.* 2011;30(6):431–451.
48. Gullstrand A. Neue methoden der reflexlosen ophthalmoskopie. *Berichte Dtsch Ophthalmol Gesellschaft.* 1910;36:326.
49. Postnov DD, Cheng X, Erdener SE, Boas DA. Choosing a laser for laser speckle contrast imaging. *Sci Rep.* 2019;9(1):2542.
50. Dhalla A-H, Migacz JV, Izatt JA. Crosstalk rejection in parallel optical coherence tomography using spatially incoherent illumination with partially coherent sources. *Opt Lett.* 2010;35(13):2305–2307.
51. Gardner M, Katta N, Rahman A, Rylander H, Milner T. Design considerations for murine retinal imaging using scattering angle resolved optical coherence tomography. *Appl Sci.* 2018;8(11):2159.
52. American National Standards Institute. *ANSI Z80.36-2016: American National Standard for Opthalmics - Light Hazard Protection for Ophthalmic Instruments*. New York: American National Standards Institute; 2016.
53. Wang J-J, Flewitt JA, Shrive NG, Parker KH, Tyberg JV. Systemic venous circulation. Waves propagating on a windkessel: relation of arterial and venous windkessels to systemic vascular resistance. *Am J Physiol Circ Physiol.* 2006;290(1):H154–H162.
54. Pagel PS, Grossman W, Haering JM, Warltier DC. Left ventricular diastolic function in the normal and diseased heart: perspectives for the anesthesiologist (second of two parts). *Anesthesiology*. 1993;79:1104–1120.
55. Yang CF, Yu-Chih Chen M, Chen TI, Cheng CF. Dose-dependent effects of isoflurane on cardiovascular function in rats. *Tzu Chi Med J.* 2014;26(3):119–122.
56. Reddy AK, Namiranian K, Lloyd EE, Bryan RM, Taffet GE, Hartley CJ. Effect of isoflurane on aortic impedance in mice. *Annu Int Conf IEEE Eng Med Biol Soc.* 2009;2009:1104–1105.
57. Ríha H, Papoušek F, Neckár J, Pirk J, Oštádal B. Effects of isoflurane concentration on basic echocardiographic parameters of the left ventricle in rats. *Physiol Res.* 2012;61(4):419–423.
58. Wang L, Pickwell-MacPherson E, Liang YP, Zhang YT. Noninvasive cardiac output estimation using a novel photoplethysmogram index. *Annu Int Conf IEEE Eng Med Biol Soc.* 2009;2009:1746–1749.
59. Mok Ahn J. New aging index using signal features of both photoplethysmograms and acceleration plethysmograms. *Healthc Inform Res.* 2017;23:53–59.
60. Elgendi M. On the analysis of fingertip photoplethysmogram signals. *Curr Cardiol Rev.* 2012;8(1):14–25.
61. Takazawa K, Tanaka N, Fujita M, et al. Assessment of vasoactive agents and vascular aging by the second derivative of photoplethysmogram waveform. *Hypertension.* 1998;32(2):365–370.
62. Imanaga I, Hara H, Koyanagi S, Tanaka K. Correlation between wave components of the second derivative of plethysmogram and arterial distensibility. *Jpn Heart J.* 1998;39(6):775–784.
63. Rubins U, Grabovskis A, Grube J, Kukulis I. Photoplethysmography analysis of artery properties in patients with cardiovascular diseases. In: Katashev A, Dekhtyar Y, Spigulis J, eds., *14th Nordic-Baltic Conference on Biomedical Engineering and Medical Physics. IFMBE Proceedings, Vol. 20*. Heidelberg: Springer; 2008:319–322.
64. Alty SR, Angarita-Jaimes N, Millasseau SC, Chowienczyk PJ. Predicting arterial stiffness from the digital volume pulse waveform. *IEEE Trans Biomed Eng.* 2007;54(12):2268–2275.
65. Wieling W, Jardine DL, de Lange FJ, et al. Cardiac output and vasodilation in the vasovagal response:

An analysis of the classic papers. *Heart Rhythm.* 2016;13(3):798–805.
66. Briers JD, Fercher AF. Retinal blood-flow visualization by means of laser speckle photography. *Invest Ophthalmol Vis Sci.* 1982;22(2):255–259.
67. Tamaki Y, Araie M, Kawamoto E, Eguchi S, Fujii H. Noncontact, two-dimensional measurement of retinal microcirculation using laser speckle phenomenon. *Invest Ophthalmol Vis Sci.* 1994;35(11):3825–3834.
68. Tamaki Y, Araie M, Kawamoto E, Eguchi S, Fujii H. Non-contact, two-dimensional measurement of tissue circulation in choroid and optic nerve head using laser speckle phenomenon. *Exp Eye Res.* 1995;60(4):373–383.
69. Ponticorvo A, Cardenas D, Dunn AK, Ts'o D, Duong TQ. Laser speckle contrast imaging of blood flow in rat retinas using an endoscope. *J Biomed Opt.* 2013;18(9):090501.
70. Srienc AI, Kurth-Nelson ZL, Newman E. Imaging retinal blood flow with laser speckle flowmetry. *Front Neuroenergetics.* 2010;2:128.
71. Ho D, Zhao X, Gao S, Hong C, Vatner DE, Vatner SF. Heart rate and electrocardiography monitoring in mice. *Curr Protoc Mouse Biol.* 2011;1:123–139.
72. Tamplin MR, Broadhurst KA, Vitale AH, Hashimoto R, Kardon RH, Grumbach IM. Longitudinal testing of retinal blood flow in a mouse model of hypertension by laser speckle flowgraphy. *Transl Vis Sci Technol.* 2021;10(2):16.
73. Vaz P, Santos P, Figueiras E, Correia C, Humeau-Heurtier A, Cardoso J. Laser speckle contrast analysis for pulse waveform extraction. In: *Proceedings SPIE* 9540*,* Novel Biophotonics Techniques and Applications III*, 954007*. Bellingham, WA: SPIE; 2015.
74. Chen RC-H. Spectral and temporal interrogation of cerebral hemodynamics via high speed laser speckle contrast imaging. Milwaukee, WI: University of Wisconsin–Milwaukee; 2015. Thesis.
75. Guevara-Torres A, Joseph A, Schallek JB. Label free measurement of retinal blood cell flux, velocity, hematocrit and capillary width in the living mouse eye. *Biomed Opt Express.* 2016;7(10):4228–4249.
76. Joseph A, Chu CJ, Feng G, Dholakia K, Schallek J. Label-free imaging of immune cell dynamics in the living retina using adaptive optics. *Elife.* 2020;9:e60547.
77. Palochak CMA, Lee HE, Song J, et al. Retinal blood velocity and flow in early diabetes and diabetic retinopathy using adaptive optics scanning laser ophthalmoscopy. *J Clin Med.* 2019;8(8):1165.
78. Ploner SB, Moult EM, Choi WJ, et al. Toward quantitative optical coherence tomography angiography: visualizing blood flow speeds in ocular: Pathology using variable interscan time analysis. *Retina.* 2016;36(suppl 1):S118–S126.